

TiO₂ Phase Engineering by Millisecond Range Annealing for Highly Efficient Photocatalysis

Slawomir Prucnal,* Raul Gago, David Gonzalez Calatayud, Lars Rebohle, Maciej Oskar Liedke, Maik Butterling, Andreas Wagner, Manfred Helm, and Shengqiang Zhou



Cite This: *J. Phys. Chem. C* 2023, 127, 12686–12694



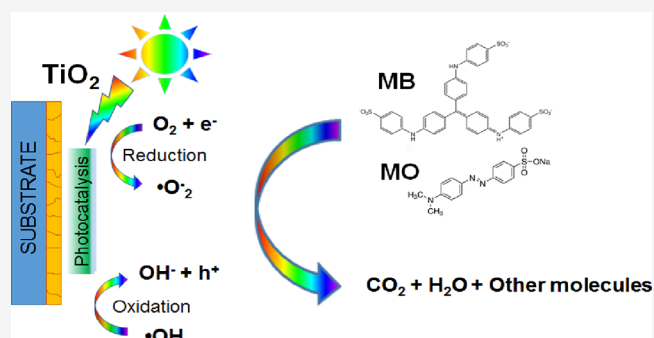
Read Online

ACCESS |

Metrics & More

Article Recommendations

ABSTRACT: Air pollution and the energy crisis are the two main driving forces behind the development of alternative, environmentally friendly methods of energy production. Photoactive materials can be used both to clean the air and to produce green hydrogen for clean energy. Transition metal oxides are one of the most considered materials for high-performance photocatalysis. In this work, we investigate the effect of millisecond flash lamp annealing (FLA) of TiO₂ on the degradation of methyl blue (MB) and methyl orange (MO). To reduce the energy consumption of the TiO₂ deposition process, the layers were made using magnetron sputtering at room temperature followed by millisecond FLA. By controlling the flash energy input, we can tune the phase formation of TiO₂ films from pure anatase to mixed anatase/rutile phases. Scanning electron microscopy, positron annihilation spectroscopy, photoluminescence, and X-ray diffraction studies show that the crystal size and film quality increase with increasing annealing temperature. Photocatalytic experiments demonstrate that FLA-treated TiO₂ films are active in degrading both MB and MO. This makes them attractive not only for the production of green hydrogen but also for the purification of water from medical contaminants.



INTRODUCTION

Metal oxides are widely used in environmental and energy fields, such as self-cleaning surfaces, air and water purification, sterilization, green-hydrogen production, and photoelectrochemical conversion.^{1–5} One of the most popular, cheap, and nontoxic materials that exhibits superior photocatalytic properties is titanium dioxide (TiO₂), also named as titania. The annual production of titania is close to 10 million tons, and it is present in two-thirds of all pigments.⁶ TiO₂ has three basic structural phases: anatase, rutile, and brookite, which determines its final optoelectronic properties. TiO₂ presents various polymorphs that are built of the same fundamental TiO₆ polyhedral building units but are connected in different ways. In all cases, a titanium cation is sixfold coordinated to the surrounding oxygen anions, forming distorted TiO₆ octahedra joined by sharing the octahedral edges and corners. Rutile and anatase present a tetragonal structure, whereas brookite has an orthorhombic unit cell. The rutile phase is the most stable one, while anatase and brookite are metastable. At elevated temperatures, the metastable phases can transform irreversibly to the rutile phase.⁷ The band gaps of anatase, rutile, and brookite TiO₂ phases are 3.2, 3.0, and 3.3 eV, respectively.⁷ The phase formation depends on the process parameters. Anatase-TiO₂ is known as a low-temperature phase, while the

rutile is the more stable phase at high temperatures (>450 °C), which results in an anatase to rutile phase transformation during annealing. Unfortunately, such transformation is not a reversible process. The critical temperature for the phase change from anatase to rutile can be tuned over a broad range, from 450 to 850 °C, by controlling the growth parameters during the TiO₂ layer deposition.^{8–10} Both the structural phases and doping have influence on the optoelectronic properties and final application of TiO₂. The disadvantage of TiO₂ for solar light harvesting is its large bandgap that allows us to absorb only about 5% of the total solar spectrum. Two of the most intriguing applications of TiO₂ are in photocatalysis (PC) and photoelectrochemistry, where the absorption of the solar energy plays a major role. Although the anatase TiO₂ has a larger band gap than rutile, it shows a much higher photocatalytic efficiency, mainly due to the longer lifetime of the photogenerated carriers caused by an indirect band gap.¹¹

Received: February 20, 2023

Revised: May 26, 2023

Published: June 22, 2023



The PC efficiency can be enhanced by (i) improving the efficiency of charge separation, (ii) surface engineering, and (iii) band gap reduction to increase the solar energy absorption, for example, by reducing TiO_2 or by doping. The former approach can be realized by increasing the average size of the nanocrystals and the reduction of the point defect concentration.¹² Surface engineering, e.g., by passivation of the dangling bonds, may reduce the probability of the non-radiative carrier recombination at the surface, enhancing the production of free radicals.¹³ The band gap reduction is one of the most common approaches to increase the PC activity of titania. It can be done by alloying TiO_2 with metals (e.g., Mn and Cr) or non-metal elements like nitrogen.^{14–18} After alloying, the band gap is reduced and, hence, it increases the visible-light absorption.¹⁹ Unfortunately, the alloying often reduces the crystal quality and the energy of photogenerated electrons, which has a negative effect on the PC efficiency. Another method to increase the PC efficiency is to increase the effective photoactive area of the film. This can be done by increasing the porosity of the active layer.²⁰ Doping engineering may also improve the PC efficiency by reducing the non-radiative recombination and increasing the carrier separation, e.g., by doping TiO_2 with donors or acceptors.^{7,21}

In this work, we present the enhancement of the PC efficiency of TiO_2 films after post-deposition millisecond-range flash lamp annealing (FLA). To reduce the energy consumption in the fabrication process, the coating is fabricated at room temperature and, subsequently, the layer is activated by FLA for 20 ms. The use of FLA saves at least 30% energy compared to the conventional heat treatment. It is shown that, using a 20 ms pulse length, the anatase phase dominates for a wide range of FLA energies, whereas the rutile transformation starts to occur at the highest values (peak surface temperatures of about 1350 °C). The enhancement of the PC efficiency is related to the increase in the average crystal size with FLA energy and the reduction of the defect concentration, the latter assessed by variable energy positron annihilation lifetime spectroscopy (VEPALS) and photoluminescence (PL) measurements. The present work opens a new road for fabrication of low-cost and high-quality titania for a more efficient utilization of solar energy.

METHODS

About 80 nm-thick TiO_2 films (measured by ellipsometry) were deposited on 275 μm -thick Si (100) substrates using reactive magnetron sputtering. Samples were deposited at room temperature (RT) using a gas mixture of Ar and O_2 at a working pressure of 0.5 Pa with an O_2 partial content of 6%. For plasma generation, a DC voltage was applied to the Ti (99.99% pure) cathode with an overall power of 150 W. The growth was performed for 120 min. After deposition, samples were annealed by FLA for 20 ms with an energy density varying from 60 to 110 Jcm^{-2} in oxygen ambient. The annealing time (20 ms) defines the full width at half-maximum of the flash pulse. The FLA system is based on Xe lamps with emission spectra in the wavelength range of about 250–800 nm.²²

The emission spectrum of the Xe lamp determines the materials, which can be effectively annealed by FLA. In principle, all solids that can absorb light at that spectral range can be effectively annealed and the maximum obtainable temperature during a single pulse is limited by the melting point of treated samples. The length of the single pulse can be

changed between 0.4 and 20 ms. In the case of TiO_2 films deposited on silicon substrates, a part of UV light was directly absorbed by the deposited film while the rest of the energy deposited onto the sample was absorbed by the substrate. Consequently, the heat from the Si substrate was back-transferred to the TiO_2 layer increasing its peak temperature. According to the COMSOL simulation,²³ the peak temperature in the TiO_2 film varies between 900 °C for the lowest annealing energy and about 1400 °C for the highest (see Figure 1). Such temperature was reached within 25 ms, and the sample then cooled down to RT in the next few seconds.

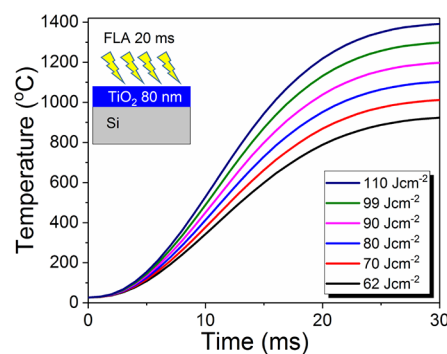


Figure 1. Temperature distribution at the surface of an 80 nm-thick TiO_2 film deposited on the 275 μm -thick Si substrate obtained by COMSOL simulation.

The structural properties of the fabricated TiO_2 films were investigated by scanning electron microscopy (SEM), X-ray diffraction (XRD) in Bragg–Brentano and grazing-incidence configurations, micro-Raman spectroscopy, and variable energy positron annihilation lifetime spectroscopy (VEPALS).²⁴ Grazing-incidence XRD measurements were carried out at an incidence angle of 0.5° using a D5000 (BRUKER AXS) diffractometer with $\text{Cu-K}\alpha$ radiation (wavelength of 1.5406 Å). Micro-Raman spectroscopy was performed at RT using a 532 nm laser for the excitation at 10 mW power focused on the spot of 1 mm diameter. The phonon spectra were recorded by liquid-nitrogen cooled Si-CCD. The open volume defects and the phase transformation in TiO_2 films, from anatase to rutile, were probed by VEPALS. The positron lifetime in the solids depends on the size of the open volume defect and increases with the size of the vacancy complex.^{25–27} Mono-energetic positrons were implanted into films with defined kinetic energies E_p that allow us to perform the depth distribution of defects. The mean positron implantation depth $\langle z \rangle$ for the material density $\rho = 4 \text{ g}\cdot\text{cm}^{-3}$ (chosen as in between the densities of the rutile and anatase phases) can be approximated as $\langle z \rangle = \frac{3.6}{\rho} E_p^{1.62}$.²⁸ For more general details about PAS, see refs 29–31. The positron lifetime experiments were performed at the mono-energetic positron spectroscopy (MePS) beam-line, at the radiation source ELBE (Electron Linac for beams with high Brilliance and low Emittance) at Helmholtz-Zentrum Dresden - Rossendorf (Germany).²⁴ A CeBr_3 scintillation detector was employed with a SPDevices ADQ14DC-2X digitizer (14-bit vertical resolution at 2 GS/s) and a dedicated software for positron annihilation lifetime data acquisition.^{31,32} The combined time resolution amounted to about 240–250 ps. The lifetime spectra were evaluated as a sum of time-dependent exponential decays, according to the equation

$$N(t) = \sum_{i=1}^{k+1} \frac{I_i}{\tau_i} e^{-t/\tau_i},$$

where $N(t)$ is the absolute value of the time derivative of the positron decay spectrum and k is the number of different defect types contributing to the positron trapping, related to $k + 1$ components in the spectra with the individual lifetimes τ_i and intensities I_i ($\sum I_i = 1$).³³ The spectra were convoluted with the spectrometer resolution function and were fitted using a non-linear least-squares fitting method in the frame of the PALSfit fitting software.³⁴ The index i gives the maximum number of the fitted discrete lifetime components τ_i (representing defect types and sizes) and their relative intensities I_i , allowing us to obtain the smallest fit standard deviation. The relative intensities can be associated to defect densities as long as positron trapping yields are in the similar range.³³ Doppler broadening variable energy positron annihilation spectroscopy (DB-VEPAS) measurements were conducted at the apparatus for in situ defect analysis (AIDA)²⁹ of the slow positron beamline (SPONSOR).³⁰ Similarly to VEPALS, DB-VEPAS allows for depth profiling, but instead of the positron lifetime acquisition, the energetics of the annihilation events were analyzed, namely, the energy distribution (its broadening, Doppler shift, compared to the ideal 511 keV annihilation line) of the released gamma radiation from the positron–electron interaction. Here, we take an advantage of the so-called S -parameter, which is defined as a fraction ratio of the annihilation spectrum in the middle region (in our case, 511 ± 0.74 keV) to the whole spectrum. The S -parameter represents annihilation with low momentum electrons, hence is a fingerprint of vacancy like defects and their concentration.³⁵

Moreover, we have performed PL measurements. PL is a well-established technique to study the optical properties and crystal quality of solids. In general, the PL intensity increases with increasing the crystal quality and decreasing the defect density. Moreover, the PL can be used to investigate the phase change in the solids, e.g., in TiO_2 , due to the change of band gap and radiative decay channels. Samples were excited with a He–Cd laser operated at 325 nm with a laser power of 20 mW. The PL signal was detected by a Si-photomultiplier at RT with a Horiba i550 spectrometer.

The photocatalytic (PC) experiments were performed using a high-pressure mercury vapor lamp for UV–visible irradiation (250 W, HPL-N Philips, Amsterdam, The Netherlands). The incident photon flux was 3.13×10^{-6} Einstein $\text{cm}^{-2} \text{s}^{-1}$, with a temperature of 25 °C. We tested the photodegradation of aqueous solutions of methyl blue (MB) and methyl orange (MO). The concentration of MB and MO was 10^{-2} mol/ cm^3 . The 10×10 mm Si substrates with 80 nm-thick photoactive TiO_2 layers were initially immersed in 10 mL of the aqueous solutions of MB or MO using a quartz beaker. The suspension, kept under magnetic stirring, was then irradiated. Aliquots were taken progressively from the suspension after different irradiation times. The absorption spectrum of the supernatant solution was measured on the spectrometer, and the concentration (degradation) of MB and MO was determined by monitoring the changes in absorbance at 655 and 460 nm, respectively. On collecting these data, two side effects were considered to avoid misinterpretation of the reduced value in the MB and MO concentrations: the self-degradation of the molecules under the irradiation and/or their adsorption on the

surface of the materials. Both scenarios were contemplated as follows:³⁶ (i) blank solutions of MB and MO with no catalysts were irradiated under the same experimental conditions; as it was observed, no degradation of phenol occurred; (ii) solutions of MB and MO with the photocatalysts were not subjected to irradiation (dark conditions), and no changes in the MB and MO concentrations were observed. The experiments were repeated three times observing in all cases a statistical uncertainty below 1%.

RESULTS AND DISCUSSION

Structural Properties. The crystallization of the TiO_2 film upon FLA was investigated using XRD. Figure 2a shows the

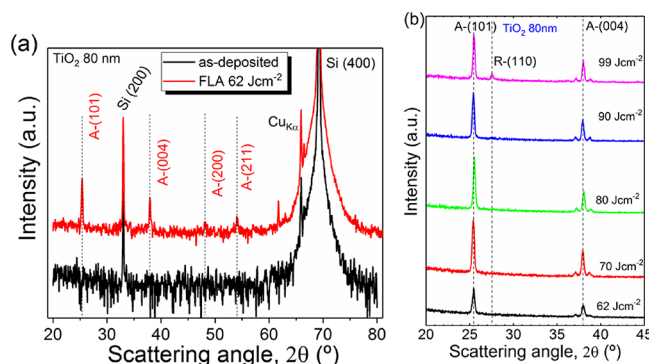


Figure 2. (a) XRD pattern of the virgin and flash lamp annealed for 20 ms TiO_2 films in Bragg–Brentano configuration. (b) Grazing-incidence XRD for TiO_2 films annealed with different energy densities. All diffractograms were shifted vertically for better visibility, and all diffractograms are not normalized. The A and R labels are for anatase and rutile phases of TiO_2 , respectively.

2θ - θ scan obtained from as-deposited and FLA-treated samples for 20 ms at an energy density of 62 Jcm^{-2} . Since the TiO_2 was deposited on the Si substrate, the XRD pattern of the as-deposited sample shows only strong peaks at about 2θ angles of 33 ± 0.02 and $69 \pm 0.02^\circ$ due to (200) and (400) reflections from the Si substrate, respectively. After FLA annealing, the XRD pattern reveals a few new peaks at about 2θ angles of 25.45 ± 0.02 , 37.90 ± 0.02 , 48.20 ± 0.02 , and $55.07 \pm 0.02^\circ$ that, according to the JCPDS card 75-1537, were assigned to the (101), (004), (200), and (211) reflections of the anatase phase of TiO_2 , respectively. The XRD results confirm that the FLA at 62 Jcm^{-2} is sufficient to recrystallize the TiO_2 layer and that only the anatase phase is formed. According to the COMSOL simulation (see Figure 1), the temperature at the sample surface during flash pulse for 20 ms with an energy density of 62 Jcm^{-2} reaches about 900°C . To study the effect of the FLA energy on the phase formation, Figure 2b shows the grazing-incidence XRD measurements for samples annealed at different energy densities for 20 ms. With increasing the flash pulse energy densities from 62 to 90 Jcm^{-2} (temperature increases from 900 to 1200°C), the crystallinity of the annealed film improves but only the anatase phase is recorded.

Only the sample annealed with a flash energy higher than 90 Jcm^{-2} indicates the formation of mixed anatase/rutile phases, as revealed by the characteristic peak in the XRD pattern for a 2θ angle at about $27.50 \pm 0.02^\circ$, corresponding to the (110) reflection from rutile TiO_2 .⁸ The average crystal size is determined from the peak position and full width at half-

maximum of the A (101) peak using the Scherrer equation.³⁷ The results are average values taking into account the layer thickness and fine grains between big crystallites. It should also be noted that other factors may contribute to peak broadening (e.g., strain), which may result in an underestimation of grain size. In any case, as the flash energy density increases, the crystal size increases from 27 to 35 nm.

The recrystallization process was monitored also by micro-Raman spectroscopy. Moreover, Raman spectroscopy also provides information about in-plane strain. Figure 3 shows the

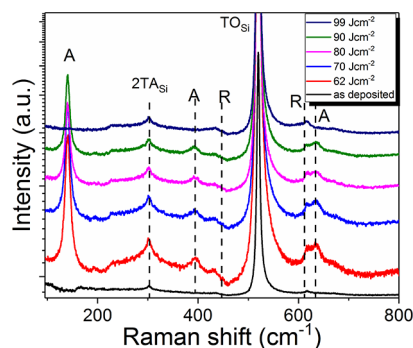


Figure 3. Micro-Raman spectra of as-deposited and annealed TiO₂ films. Samples were annealed for 20 ms with different energies as indicated in the figure. Peak positions for the rutile and anatase phonon modes are marked with R and A, respectively. 2TA and TO are the second-order transverse acoustic and transverse optical phonon modes in the silicon substrate, respectively.

micro-Raman spectra obtained from as-deposited and annealed TiO₂ films on the Si substrate. Similar to XRD data, the as-deposited sample shows only two peaks due to the phonon vibrations in the silicon substrate.³⁸ The vibration mode at $303 \pm 0.2 \text{ cm}^{-1}$ is due to the second-order transverse acoustic phonon mode (2TA), and the main peak at $520 \pm 0.2 \text{ cm}^{-1}$ corresponds to the transverse optical (TO) mode. After annealing with an energy density of 62 Jcm^{-2} , the new phonon mode at about $142 \pm 0.2 \text{ cm}^{-1}$ is observed, which is due to the ¹E_g phonon vibration mode in the anatase phase (A).³⁹ Anatase TiO₂ shows also two more relative weak phonon modes at about $394 \pm 0.2 \text{ cm}^{-1}$ (B_{1g} phonon mode) and $635 \pm 0.2 \text{ cm}^{-1}$ (³E_g).⁴⁰ With increasing the annealing energy, a new phonon vibration mode (R) at about 612 cm^{-1} is detected. The A_{1g} phonon mode at $612 \pm 0.2 \text{ cm}^{-1}$ is a fingerprint of the rutile TiO₂.⁴⁰ The coexistence of both A and R modes in the samples annealed at higher energies suggests the formation of either anatase TiO₂ with rutile inclusions (lower annealing energy) or the rutile phase with anatase inclusions for the highest annealing energy density.

To investigate the evolution of the structural defects before and after FLA annealing of TiO₂, we have performed VEPALS measurements. It is one of the most sensitive techniques to identify open volume defects with a size sensitivity down to a single missing atom. TiO₂/Si samples were implanted with positrons with discrete kinetic energies up to 11.6 keV (1.4–11.6 keV) that correspond to a positron penetration depth of about 477 nm for TiO₂. Since the TiO₂ layer is only 80 nm thick, the TiO₂-related signal is registered for positron energies below 4 keV and the remaining signal for a larger E_p originates from the increasing positron fraction annihilating in the Si substrate. The measured positron annihilation lifetimes were fitted with two exponential components τ_1 and τ_2 . The lifetime

τ_1 corresponds to the positrons that annihilate in mono- and divacancies, while τ_2 is the annihilation time in larger open volume defects V_n, i.e., vacancy agglomerations with $n > 3$ vacancies within a cluster. The change of the τ_1 component with increasing temperature can be used to determine the transition temperature for the formation of anatase or rutile phases in the crystal since the density for both materials increases from 3.89 g/cm^3 in anatase to 4.23 g/cm^3 in rutile. This strongly affects the size of the small vacancy clusters $n \leq 2$ and shortens the bond lengths between two Ti atoms.⁴¹ According to the literature, the positron annihilation lifetime in good quality anatase is around 200 ps and is reduced to about 135 ps for the perfect rutile crystal.⁴² Since the bulk positron lifetime in a defect free rutile TiO₂ is about $\tau_B \approx 148 \text{ ps}$, lifetimes lower than this value are considered as reduced and indicate simultaneous positron annihilation at interstitial positions and inside a single defect type. The positron annihilation lifetimes of about 330–350 and $230 \pm 10 \text{ ps}$ are due to positron annihilation in trivacancies in the anatase phase and close to the size of divacancy in the rutile phase, respectively. Therefore, the τ_1 component can be also used to analyze the phase transformation in annealed TiO₂ films. On the other hand, the τ_2 component (Figure 4b) describes the evolution of larger open volume defects, e.g., vacancy agglomerations and microvoids at grain boundaries and their intersections. The τ_2 longer than 500 ps corresponds usually to small micropores. The lifetime τ_1 presented in Figure 4a shows a significant change of the defect structure after annealing. According to Figure 4b, the τ_2 component decreases with increasing the annealing temperature as well. It is likely due to the increase in the average size of the nanocrystals and concomitant reduction of the defect size (possibly at grain boundaries at least in the anatase phase).

Figure 4c and Figure 4d present the relative intensity of the annihilation fraction of positrons with lifetimes τ_1 and τ_2 , respectively. The decrease in I_1 and simultaneous increase in I_2 mean that, with increasing the annealing temperature (flash energy density), the concentration of positrons that annihilates within nanocrystals (defects) decreases and more positrons annihilate at grain boundaries. The former is often due to annealing effects; hence, more positrons can diffuse to grain boundaries. In Figure 4e, both lifetime components τ_1 and τ_2 , as well as the so-called average positron lifetime τ_{av} (average defect size), and I_1 all taken at 2.3 keV are plotted. The chosen energy corresponds to the average depth close to the middle of the TiO₂ layer. It is well visible that, for a flash energy density of $80\text{--}90 \text{ Jcm}^{-2}$, there are stronger deviations, which could be ascribed to the transition from the anatase-rich to the rutile-rich phase, in agreement with XRD and micro-Raman spectroscopy. τ_{av} strongly indicates that before and after the transition, the average defect size changes stepwise and is reduced in the rutile-rich phase. The sudden jump of I_1 likely reflects a regrowth and size expansion of the crystallites, limiting positrons' reach to grain boundaries. The subsequent drop of I_1 indicates further annealing of the τ_1 -related defects due to increasing temperature. Figure 4f shows the change of the S-parameter as a function of the positron implantation energy ($S(E_p)$) for all samples measured by DB-VEPAS. The change of the absolute value of S indicates the change of the defect density. In our case, the slope of the $S(E_p)$ slightly decreases with increasing the flash energy density up to 90 Jcm^{-2} , but at the same time, S is reduced as well. The decrease in S is an indication of a lower effective defect concentration.

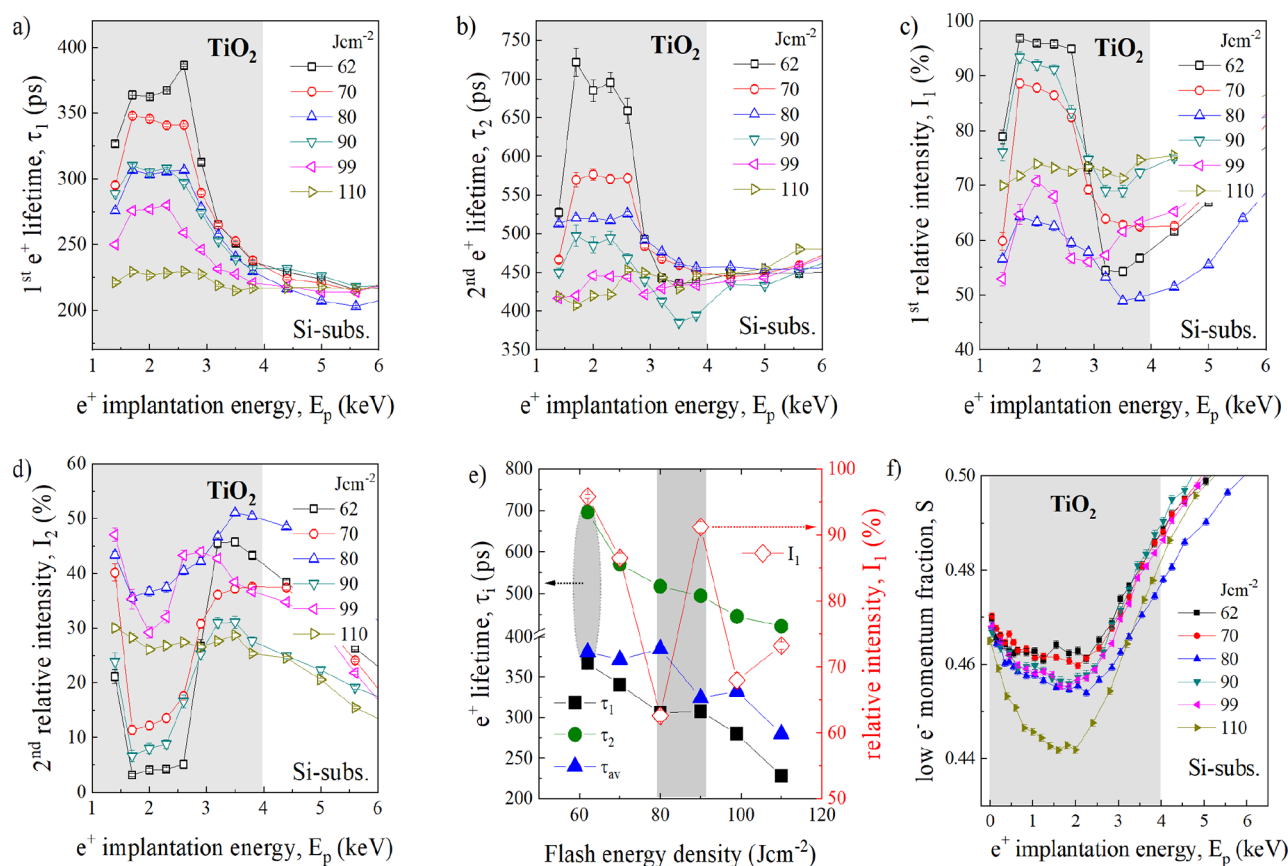


Figure 4. VEPALS data recorded from annealed TiO₂ films deposited on the Si substrate, where panels (a, b) present the τ_1 and τ_2 components of the positron annihilation lifetimes, respectively. (c, d) Relative intensity I_1 and I_2 for positrons that annihilate with τ_1 and τ_2 , respectively. (e) Lifetime components τ_1 and τ_2 , as well as average positron lifetime τ_{av} (average defect size), and I_1 all taken at 2.3 keV for samples annealed at different flash energy densities and (f) S-parameter as a function of positron implantation energy measured by DB-VEPAS. The positrons implanted with an energy larger than ~ 4 keV are partially stopped in the silicon substrate (white part of the graph). The film region is marked in gray.

Since the crystallites are much larger at 90 Jcm⁻², the relative fraction of positrons that can annihilate with their boundaries is lower. As shown by XRD, the average size of crystals increases with increasing the annealing temperature and, hence, the volume of open defects at grain boundaries where positrons can annihilate with τ_2 should also decrease. Therefore, the crystal quality of TiO₂ increases by increasing flash energy densities.

A further verification of the evolution of the grain size after FLA was obtained with SEM. The resulting images are presented in Figure 5, which show the lateral crystal size evolution with increasing the FLA energy density. The

topography visible in the SEM images is most probably due to the formation of agglomerated crystallites with cracks formed due to the different expansion coefficients of TiO₂ and Si. For the lowest energy density of 62 Jcm⁻² (~ 900 °C), the image displays a fine-grained structure with an average crystal size in the range of 10–30 nm (about 27 nm according to XRD). Next, the agglomerated grains grow to about 30–60 nm for a flash energy density of 70 Jcm⁻². Increasing the flash energy density to about 90 Jcm⁻², the average agglomerated grains increase to about 100–200 nm and, finally, annealing with an energy density of 99 Jcm⁻² causes the formation of TiO₂ films with agglomerates larger than 200 nm containing crystallites with an average size of about 35 nm.

Optical Properties. In the case of anatase TiO₂, the main emission is in the visible spectral range at about 2.3–2.5 eV, while the rutile phase shows a PL emission at about 1.3–1.5 eV.^{43–48}

The as-deposited sample shows very weak luminescence at about 420 nm (2.95 eV) (see Figure 6). After annealing with the lowest energy density, the main PL emission significantly increases and is red-shifted with a peak at 522 nm (2.36 eV). With increasing the annealing temperature (flash energy density), the PL intensity increases even more and the PL peak shifts slightly to a shorter wavelength by 15 nm. Interestingly, we do not see the characteristic near-infrared PL emission from rutile TiO₂ even after annealing at the highest flash energy density and despite the fact that both

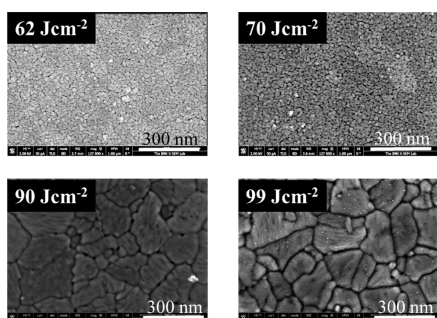


Figure 5. SEM images of FLA-treated TiO₂ films with different energy densities.

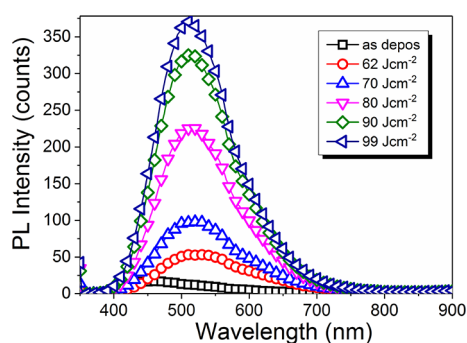


Figure 6. Photoluminescence spectra obtained from TiO₂ films after 325 nm laser excitation at RT with a laser power density of 20 mW. Samples were annealed by FLA for 20 ms at different energy densities.

micro-Raman and XRD confirm the existence of the rutile phase. The green photoluminescence from anatase TiO₂ is due to the radiative recombination of self-trapped excitons created by spontaneous self-localization of photogenerated carriers, typically appearing in polar semiconductors with strong electron–phonon coupling like XTiO₃ (X = Mg, Ba, and Sr).^{48,49} According to the PL and PL-excitation experiments presented by Pallotti et al.,⁴⁴ the green luminescence in anatase TiO₂ is due to the radiative recombination of photogenerated conduction band electrons with self-trapped holes. They have shown that in the PL performed in the oxidation media (UV irradiation in an oxygen atmosphere), the green luminescence is strongly quenched. The chemisorbed O₂ molecules at the TiO₂ surface attract the photogenerated conduction band electrons that reduce the concentration of self-trapped excitons and lead to the formation of oxygen free radicals like the superoxide anion radical (O₂^{•−}). Therefore, samples with bright green photoluminescence are attractive for photocatalysis, e.g., photodegradation of organic pollutants, green hydrogen production, or antiseptic coatings.⁵⁰

Photocatalytic Properties. The influence of the FLA upon different parameters on the photocatalysis was tested using two different organic dyes, methyl blue (MB) and methyl orange (MO). MB is a dye that is commonly used in the literature to evaluate the degradation of pollutants, and that allows us to estimate initially whether a compound is photoactive or not since it is an easily degradable molecule. On the other hand, and seeking to use a real pollutant, the photocatalytic activity has also been evaluated using MO. MO is a common anionic azo dye that is harmful to the environment and biology, so it must be treated innocuously before it can be discharged. MO is a synthetic azo dye, which is one of the important dyes that is generally used as a coloring agent in textile and leather industries.⁵¹ It is widely used in printing, paper manufacturing, pharmaceutical, food processing industries, and in research laboratories.^{52,53} Figure 7 shows the photoactivity for all the samples for the degradation of MO and MB. As observed, the photocatalytic activity in the degradation of both molecules improves as the annealing energy densities increased until a maximum improvement is reached, which in both cases is at 70–80 Jcm^{−2}. A further increase in the annealing temperature does not noticeably improve the PC performance. The initial enhancement of the PC efficiency with increasing the FLA energy density can be justified by the improvement in the crystallinity of the films, which favors photoactivity and reduces the non-radiative recombination channels for photoexcited carriers. The best and

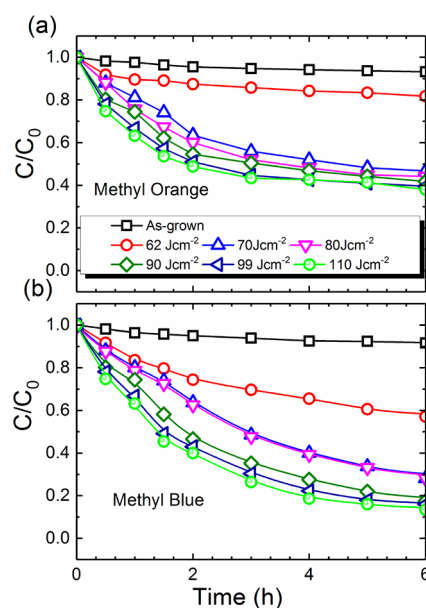


Figure 7. (a, b) Photodegradation of MB and MO using TiO₂ films under irradiation.

reference PC performance was observed for TiO₂ powders with mixed phases like commercial photocatalyst Degussa P-25 with 25% of rutile and 75% of anatase crystallites.⁵⁰ Therefore, samples with mixed phases can be favorable to promote the PC activity. Moreover, the PC activity of different phases also depends on the crystal orientation. The best performance was observed for anatase with {101} facets and rutile with {011} and {110} crystal facets.^{54,55} The {101} facets are thermodynamically stable with 50% Ti fivefold coordinated, Ti_{5c}, and 50% Ti sixfold coordinated, Ti_{6c}, while anatase-TiO₂ with {001} facets is more reactive due to the surface with 100% Ti_{5c}. Unfortunately, during recrystallization under annealing in thermodynamic equilibrium conditions like rapid thermal annealing or furnace annealing, the {001} facets dominate only in the first stages of the crystallization process. In our case, the strongly non-equilibrium annealing process at milliseconds may favor the formation of {001} facets instead of {101} facets, even after annealing at the highest temperature. Recently, we have demonstrated the formation of different metastable phases in various alloys synthesized by millisecond-range FLA through explosive solid phase recrystallization, e.g., B20-MnSi and Mn₅Ge₃.^{56,57} In general, during explosive solid phase recrystallization, it is possible to obtain compounds and crystals that only form under extreme conditions, e.g., high pressure and temperature.

Moreover, as seen in SEM images, the synthesized films have a rough surface that increases the effective surface area for PC and can promote the TiO₂ anatase with {001} facets. The fact that the photoactivity does not improve with the increase in crystallinity of the samples treated at higher energy densities can be justified by an increase in the rutile fraction in the film. As can be seen, the reaction kinetics is faster for MB. However, in the case of MO, after 6 h, the photodegradation slows down, probably due to the passivation of the catalyst surface by the formation of secondary species during the degradation of MO. Here, we have tested an almost flat TiO₂ film with an active surface area of about 100 mm² and total weight of TiO₂ of about 0.32 μg that is a few orders of magnitude less than the typical amount of the photoactive material used for the PC test

(usually between 2 mg and 0.2 g).⁵⁸ Although, these results confirm the successful fabrication of films with improved photoactivity, suitable for the removal of pollutants in water, and with the photocatalyst completely immobilized on the substrate. Since the TiO₂ is immobilized, it can be used also for air purification and presented technology can be implemented to the photoactive-antibacterial coatings in clinical application as the passive layer to reduce hospital-acquired infections.

CONCLUSIONS

We have developed a cost-effective procedure to fabricate TiO₂ films that show superior PC response to the bleaching of both acidic/anionic (MO) and basic/cationic (MB) dyes. The anatase- or rutile-rich TiO₂ layers are made by RT deposition and recrystallization by post-deposition annealing with millisecond-range intense light pulses. Due to the short processing time, the anatase phase is present in the film for annealing temperatures higher than 1200 °C. The formation of relatively large crystals with a reduced defect concentration increases the lifetime of self-trapped excitons, which can be related to the improvement in the PC efficiency. The presented technology for the TiO₂ layer with superior photocatalytic response is attractive for the degradation of indoor air pollution like nicotine and biological contaminants including bacteria and viruses.

AUTHOR INFORMATION

Corresponding Author

Slawomir Prucnal – Helmholtz-Zentrum Dresden-Rossendorf, Institute of Ion Beam Physics and Materials Research, 01328 Dresden, Germany; orcid.org/0000-0002-4088-6032; Email: s.prucnal@hzdr.de

Authors

Raul Gago – Instituto de Ciencia de Materiales de Madrid, Consejo Superior de Investigaciones Científicas, E-28049 Madrid, Spain

David Gonzalez Calatayud – Instituto de Cerámica y Vidrio Consejo Superior de Investigaciones Científicas, E-28049 Madrid, Spain; Departamento de Química Inorgánica, Facultad de Ciencias, Universidad Autónoma de Madrid, E-28049 Madrid, Spain; orcid.org/0000-0003-2633-2989

Lars Rebohle – Helmholtz-Zentrum Dresden-Rossendorf, Institute of Ion Beam Physics and Materials Research, 01328 Dresden, Germany

Maciej Oskar Liedke – Helmholtz-Zentrum Dresden-Rossendorf, Institute of Radiation Physics, 01328 Dresden, Germany; orcid.org/0000-0001-7933-7295

Maik Butterling – Helmholtz-Zentrum Dresden-Rossendorf, Institute of Radiation Physics, 01328 Dresden, Germany

Andreas Wagner – Helmholtz-Zentrum Dresden-Rossendorf, Institute of Radiation Physics, 01328 Dresden, Germany

Manfred Helm – Helmholtz-Zentrum Dresden-Rossendorf, Institute of Ion Beam Physics and Materials Research, 01328 Dresden, Germany

Shengqiang Zhou – Helmholtz-Zentrum Dresden-Rossendorf, Institute of Ion Beam Physics and Materials Research, 01328 Dresden, Germany; orcid.org/0000-0002-4885-799X

Complete contact information is available at:
<https://pubs.acs.org/10.1021/acs.jpcc.3c01165>

Author Contributions

S.P. designed the research question, supervised the project, and was responsible for the flash lamp annealing and optical characterizations, R.G. deposited the TiO₂ layers and performed XRD and SEM, D.G.C. made the PC tests, M.O.L., M.B., and A.W. were responsible for PALS, and all co-authors read, edited, and approved the final manuscript.

Notes

The authors declare no competing financial interest.

ACKNOWLEDGMENTS

This research has received funding from grant TED2021-129876B-I00 of the Ministerio de Ciencia, Innovación y Universidades (Spain). We also acknowledge the use of the SEM facility at the MiNa Laboratory of Instituto de Micro y Nanotecnología (CSIC) and the technical assistance of Dr. Esteban-Mendoza during the measurements. Parts of this research were carried out at ELBE at the Helmholtz-Zentrum Dresden - Rossendorf e.V., a member of the Helmholtz Association. We would like to thank the facility staff (Ahmed G. Attallah and Eric Hirschmann) for assistance. This work was partially supported by the Impulse-und Net-working fund of the Helmholtz Association (FKZ VH-VI-442 Memriox) and the Helmholtz Energy Materials Characterization Platform (03ET7015).

REFERENCES

- (1) Liu, Y.; Li, Z.; Green, M.; Just, M.; Li, Y. Y.; Chen, X. Titanium Dioxide Nanomaterials for Photocatalysis. *J. Phys. D: Appl. Phys.* **2017**, *50*, No. 193003.
- (2) Ghosh, S.; Kouamé, N. A.; Ramos, L.; Remita, S.; Dazzi, A.; Deniset-Besseau, A.; Beaunier, P.; Goubard, F.; Aubert, P.-H.; Remita, H. Conducting Polymer Nanostructures for Photocatalysis under Visible Light. *Nat. Mater.* **2015**, *14*, 505–511.
- (3) Khanchandani, S.; Kumar, S.; Ganguli, A. K. Comparative Study of TiO₂/CuS Core/Shell and Composite Nanostructures for Efficient Visible Light Photocatalysis. *ACS Sustainable Chem. Eng.* **2016**, *4*, 1487–1499.
- (4) Wang, W.; Tadé, M. O.; Shao, Z. Research Progress of Perovskite Materials in Photocatalysis- and Photovoltaics-Related Energy Conversion and Environmental Treatment. *Chem. Soc. Rev.* **2015**, *44*, 5371–5408.
- (5) Fei, J.; Li, J. Controlled Preparation of Porous TiO₂-Ag Nanostructures through Supramolecular Assembly for Plasmon-Enhanced Photocatalysis. *Adv. Mater.* **2015**, *27*, 314–319.
- (6) Titanium Dioxide Market Size, Share & Trends [2023 Report]. www.grandviewresearch.com/industry-analysis/titanium-dioxide-industry#. (accessed 2023-05-26).
- (7) Guo, Q.; Zhou, C.; Ma, Z.; Yang, X. Fundamentals of TiO₂ Photocatalysis: Concepts, Mechanisms, and Challenges. *Adv. Mater.* **2019**, *31*, 1901997.
- (8) Hanaor, D. A. H.; Sorrell, C. C. Review of the Anatase to Rutile Phase Transformation. *J. Mater. Sci.* **2010**, *46*, 855–874.
- (9) Zhang, Q.; Li, C. High Temperature Stable Anatase Phase Titanium Dioxide Films Synthesized by Mist Chemical Vapor Deposition. *Nanomaterials* **2020**, *10*, 911.
- (10) Gago, R.; Prucnal, S.; Esteban-Mendoza, D. Soft X-Ray Absorption Study of Tantalum Incorporation in Titanium Oxide Films: Impact of Flash-Lamp Annealing. *Ceram. Int.* **2020**, *46*, 15772–15778.
- (11) Žerjav, G.; Žižek, K.; Zavašnik, J.; Pintar, A. Brookite vs. Rutile vs. Anatase: What's behind Their Various Photocatalytic Activities? *J. Environ. Chem. Eng.* **2022**, *10*, No. 107722.
- (12) He, S.; Meng, Y.; Cao, Y.; Huang, S.; Yang, J.; Tong, S.; Wu, M. Hierarchical Ta-Doped TiO₂ Nanorod Arrays with Improved Charge

Separation for Photoelectrochemical Water Oxidation under FTO Side Illumination. *Nanomaterials* **2018**, *8*, 983.

(13) Gago, R.; Vinnichenko, M.; Redondo-Cubero, A.; Czizgany, Z.; Vázquez, L. Surface Morphology of Heterogeneous Nanocrystalline Rutile/Amorphous Anatase TiO₂ Films Grown by Reactive Pulsed Magnetron Sputtering. *Plasma Processes Polym.* **2010**, *7*, 813–823.

(14) Gago, R.; Prucnal, S.; Hübner, R.; Munnik, F.; Esteban-Mendoza, D.; Jiménez, I.; Palomares, J. Phase Selectivity in Cr and N Co-Doped TiO₂ Films by Modulated Sputter Growth and Post-Deposition Flash-Lamp-Annealing. *Coatings* **2019**, *9*, 448.

(15) Gago, R.; Prucnal, S.; Pérez-Casero, R.; Caretti, I.; Jiménez, I.; Lungwitz, F.; Cornelius, S. Structural Impact of Chromium Incorporation in As-Grown and Flash-Lamp-Annealed Sputter Deposited Titanium Oxide Films. *J. Alloys Compd.* **2017**, *729*, 438–445.

(16) Xie, W.; Li, R.; Xu, Q. Enhanced Photocatalytic Activity of Se-Doped TiO₂ under Visible Light Irradiation. *Sci. Rep.* **2018**, *8*, 8752.

(17) Gago, R.; Redondo-Cubero, A.; Vinnichenko, M.; Lehmann, J.; Munnik, F.; Palomares, F. J. Spectroscopic Evidence of NO_x Formation and Band-Gap Narrowing in N-Doped TiO₂ Films Grown by Pulsed Magnetron Sputtering. *Mater. Chem. Phys.* **2012**, *136*, 729–736.

(18) Mwabora, J. M.; Lindgren, T.; Avendaño, E.; Jaramillo, T. F.; Lu, J.; Lindquist, S.-E.; Granqvist, C.-G. Structure, Composition, and Morphology of Photoelectrochemically Active TiO_{2-x}N_x Thin Films Deposited by Reactive DC Magnetron Sputtering. *J. Phys. Chem. B* **2004**, *108*, 20193–20198.

(19) Assadi, M. H. N.; Hanaor, D. A. H. The Effects of Copper Doping on Photocatalytic Activity at (101) Planes of Anatase TiO₂: A Theoretical Study. *Appl. Surf. Sci.* **2016**, *387*, 682–689.

(20) Rico, V. J.; Turk, H.; Serna, R.; González-Elipe, A. R. Titania Enhanced Photocatalysis and Dye Giant Absorption in Nanoporous 1D Bragg Microcavities. *ACS Appl. Nano Mater.* **2022**, *5*, 5487–5497.

(21) Yu, Z.; Guo, H.; Sun, Z.; Li, Y.; Liu, Y.; Yang, W.; Zhu, M.; Jin, H.; Li, Y.; Feng, L.; et al. U7Co 3d Impurity Energy Level Mediated Photogenerated Carriers Transfer in Bi₂S₃/ZnS:Co/TiO₂ Photoanode. *Chem. Eng. J.* **2022**, *433*, No. 134458.

(22) Prucnal, S.; Rebohle, L.; Skorupa, W. Doping by Flash Lamp Annealing. *Mater. Sci. Semicond. Process.* **2017**, *62*, 115–127.

(23) COMSOL® Software Version 6.0 Release Highlights. COMSOL. <https://www.comsol.com/release/6.0> (accessed 2023-05-26).

(24) Wagner, W.; Butterling, M.; Liedke, M. O.; Potzger, K.; Krause-Rehberg, R. Positron annihilation lifetime and Doppler broadening spectroscopy at the ELBE facility. *AIP Conf. Proc.* **2018**, *1970*, No. 040003.

(25) Ghosh, S.; Khan, G. G.; Mandal, K.; Samanta, A.; Nambissan, P. M. G. Evolution of Vacancy-Type Defects, Phase Transition, and Intrinsic Ferromagnetism during Annealing of Nanocrystalline TiO₂ Studied by Positron Annihilation Spectroscopy. *J. Phys. Chem. C* **2013**, *117*, 8458–8467.

(26) Luo, C.; Ren, X.; Dai, Z.; Zhang, Y.; Duesberg, G. S.; Pan, C. Present Perspectives of Advanced Characterization Techniques in TiO₂-Based Photocatalysts. *ACS Appl. Mater. Interfaces* **2017**, *9*, 23265–23286.

(27) García-Valenzuela, A.; Butterling, M.; Liedke, M. O.; Hirschmann, E.; Trinh, T. T.; Attallah, A. G.; Wagner, A.; Alvarez, R.; Gil-Rostra, J.; Rico, V.; et al. Positron Annihilation Analysis of Nanopores and Growth Mechanism of Oblique Angle Evaporated TiO₂ and SiO₂ Thin Films and Multilayers. *Microporous Mesoporous Mater.* **2020**, *295*, No. 109968.

(28) Dryzek, J.; Horodek, P. GEANT4 Simulation of Slow Positron Beam Implantation Profiles. *Nucl. Instrum. Methods Phys. Res., Sect. B* **2008**, *266*, 4000–4009.

(29) Liedke, M. O.; Anwand, W.; Bali, R.; Cornelius, S.; Butterling, M.; Trinh, T. T.; Wagner, A.; Salamon, S.; Walecki, D.; Smekhova, A.; et al. Open Volume Defects and Magnetic Phase Transition in Fe₆₀Al₄₀ Transition Metal Aluminide. *J. Appl. Phys.* **2015**, *117*, 163908–163908.

(30) Anwand, W.; Brauer, G.; Butterling, M.; Kissener, H. R.; Wagner, A. Design and Construction of a Slow Positron Beam for Solid and Surface Investigations. *Defect Diffus. Forum* **2012**, *331*, 25–40.

(31) Wagner, A.; Anwand, W.; Attallah, A. G.; Dornberg, G.; Elsayed, M.; Enke, D.; Hussein, A. E. M.; Krause-Rehberg, R.; Liedke, M. O.; Potzger, K.; et al. Positron annihilation lifetime spectroscopy at a superconducting electron accelerator. *J. Phys. Conf. Ser.* **2017**, *791*, No. 012004.

(32) Hirschmann, E.; Butterling, M.; Hernandez Acosta, U.; Liedke, M. O.; Attallah, A. G.; Petring, P.; Görler, M.; Krause-Rehberg, R.; Wagner, A. A New System for Real-Time Data Acquisition and Pulse Parameterization for Digital Positron Annihilation Lifetime Spectrometers with High Repetition Rates. *J. Instrum.* **2021**, *16*, P08001–P08001.

(33) Krause-Rehberg, R.; Leipner, H. S. “Positron Annihilation in Semiconductors: Defect Studies,” Springer-Verlag, Berlin Heidelberg, New York, 1999, p. 378.

(34) Olsen, J. V.; Kirkegaard, P.; Pedersen, N. J.; Eldrup, M. PALSfit: A new program for the evaluation of positron lifetime spectra. *Phys. Status Solidi C* **2007**, *4*, 4004.

(35) Čížek, J. Characterization of Lattice Defects in Metallic Materials by Positron Annihilation Spectroscopy: A Review. *J. Mater. Sci. Technol.* **2018**, *34*, 577–598.

(36) Calatayud, D. G.; Flores, M. R.; Castellanos-Aliaga, A.; Peiteado, M.; Palomares, F. J.; Caballero, A. C.; Jardiell, T. Tailoring the Visible Light Photoactivity of Un-Doped Defective TiO₂ Anatase Nanoparticles through a Simple Two-Step Solvothermal Process. *Nanotechnology* **2020**, *31*, No. 045603.

(37) Patterson, A. The Scherrer Formula for X-Ray Particle Size Determination. *Phys. Rev.* **1939**, *56*, 978–982.

(38) Berencén, Y.; Prucnal, S.; Möller, W.; Hübner, R.; Rebohle, L.; Schönherr, T.; Bilal, K. M.; Wang, M.; Glaser, M.; et al. Formation of n- and p-type regions in individual Si/SiO₂ core/shell nanowires by ion beam doping. *Nanotechnology* **2018**, *29*, No. 474001.

(39) Balachandran, U.; Eror, N. Raman spectra of titanium dioxide. *J. Sol. State Chem.* **1982**, *42*, 276–282.

(40) Anthony, J. W.; Bideaux, R. A.; Bladh, K. W.; Nichols, M. C. (Hrsg.): *Handbook of Mineralogy*, Mineralogical Society of America. 2001.

(41) Zheng, F.; Liu, Y.; Liu, Z.; Dai, Y.-Q.; Fang, P.-F.; Wang, S.-J. Study on defect properties of nanocrystalline TiO₂ during phase transition by positron annihilation lifetime. *J. Cryst. Growth* **2012**, *353*, 55–58.

(42) Radhika, N. V.; Venkata, S. G.; Murukeshan, V. M.; Vijayan, C. A review on optical bandgap engineering in TiO₂ nanostructures via doping and intrinsic vacancy modulation towards visible light applications. *J. Phys. D: Appl. Phys.* **2022**, *55*, No. 313003.

(43) Jin, C.; Liu, B.; Lei, Z.; Sun, J. Structure and photoluminescence of the TiO₂ films grown by atomic layer deposition using tetrakis-dimethylamino titanium and ozone. *Nanoscale Res. Lett.* **2015**, *10*, 95.

(44) Pallotti, D. K.; Passoni, L.; Maddalena, P.; Di Fonzo, F.; Lettieri, S. Photoluminescence Mechanisms in Anatase and Rutile TiO₂. *J. Phys. Chem. C* **2017**, *121*, 9011–9021.

(45) Wrana, D.; Gensch, T.; Jany, B. R.; Ciešlik, K.; Rodenbücher, C.; Cempura, G.; Kruk, A.; Krok, F. Photoluminescence imaging of defects in TiO₂: The influence of grain boundaries and doping on charge carrier dynamics. *Appl. Surf. Sci.* **2021**, *569*, No. 150909.

(46) Nakamura, R.; Nakato, Y. Primary Intermediates of Oxygen Photoevolution Reaction on TiO₂ (Rutile) Particles, Revealed by In Situ FTIR Absorption and Photoluminescence Measurements. *J. Am. Chem. Soc.* **2004**, *126*, 1290–1298.

(47) Leonelli, R.; Brebner, J. L. Time-Resolved Spectroscopy of the Visible Emission Band in Strontium Titanate. *Phys. Rev. B: Condens. Matter Mater. Phys.* **1986**, *33*, 8649–8656.

(48) Di Valentin, C.; Selloni, A. Bulk and Surface Polarons in Photoexcited Anatase TiO₂. *J. Phys. Chem. Lett.* **2011**, *2*, 2223–2228.

- (49) Luttrell, T.; Halpegamage, S.; Tao, J.; Kramer, A.; Sutter, E.; Batzill, M. Why is anatase a better photocatalyst than rutile? - Model studies on epitaxial TiO₂ films. *Sci. Rep.* **2014**, *4*, 4043.
- (50) Ohno, T.; Sarukawa, K.; Tokieda, K.; Matsumura, M. Morphology of a TiO₂ photocatalyst (Degussa, P-25) consisting of anatase and rutile crystalline phases. *J. Catal.* **2001**, *203*, 82–86.
- (51) Znad, H.; Abbas, K.; Hena, S.; Awual, M. R. Synthesis a novel multilamellar mesoporous TiO₂/ZSM-5 for photo-catalytic degradation of methyl orange dye in aqueous media. *J. Environ. Chem. Eng.* **2018**, *6*, 218–227.
- (52) Bhowmik, M.; Deb, K.; Debnath, A.; Saha, B. Mixed phase Fe₂O₃/Mn₃O₄ magnetic nanocomposite for enhanced adsorption of methyl orange dye: neural network modeling and response surface methodology optimization. *Appl. Organomet. Chem.* **2018**, *32*, No. e4186.
- (53) Sejie, F. P.; Tabbiruka, M. S. N. Removal of methyl orange (MO) from water by adsorption onto modified local clay (kaolinite). *Phys. Chem* **2016**, *6*, 39–48.
- (54) Pan, J.; Liu, G.; Lu, G. Q.; Cheng, H.-M. On the true photoreactivity order of {001}, {010}, and {101} facets of anatase TiO₂ crystals. *Angew. Chem., Int. Ed.* **2011**, *50*, 2133–2137.
- (55) Ohno, T.; Sarukawa, K.; Matsumura, M. Crystal faces of rutile and anatase TiO₂ particles and their roles in photocatalytic reactions. *New J. Chem.* **2002**, *26*, 1167–1170.
- (56) Li, Z.; Yuan, Y.; Begeza, V.; Rebohle, L.; Helm, M.; Nielsch, K.; Prucnal, S.; Zhou, S. Phase Selection in Mn–Si Alloys by Fast Solid-State Reaction with Enhanced Skyrmion Stability. *Adv. Funct. Mater.* **2021**, *31*, 2009723.
- (57) Xie, Y.; Yuan, Y.; Wang, M.; Xu, C.; Hubner, R.; Grenzer, J.; Zeng, Y.-J.; Helm, M.; Zhou, S.; Prucnal, S. Epitaxial Mn₅Ge₃ (100) layer on Ge (100) substrates obtained by flash lamp annealing. *Appl. Phys. Lett.* **2018**, *113*, No. 222401.
- (58) Adeel, M.; Saeed, M.; Khan, I.; Muneer, M.; Akram, N. Synthesis and Characterization of Co–ZnO and Evaluation of Its Photocatalytic Activity for Photodegradation of Methyl Orange. *ACS Omega* **2021**, *6*, 1426–1435.

NOTE ADDED AFTER ASAP PUBLICATION

This paper was published on June 22, 2023, with an error in an author's name. The corrected version was reposted on June 23, 2023.

Recommended by ACS

Molecular-Linked Z-Scheme Heterojunction of Ti³⁺-Doped TiO₂ and WO₃ Nanoparticles for Photocatalytic Removal of Acetaldehyde

Yeseul Hong, Hyoyoung Lee, *et al.*

JUNE 27, 2023

ACS APPLIED NANO MATERIALS

READ 

Synergy of Bulk Defects and Surface Defects on TiO₂ for Highly Efficient Photocatalytic Production of H₂O₂

Cong Fu, Xiaojun Zhang, *et al.*

AUGUST 22, 2023

THE JOURNAL OF PHYSICAL CHEMISTRY LETTERS

READ 

Modulating the Conduction Band of MOFs by Introducing Tiny TiO₂ Nanoparticles for Enhanced Photocatalytic Performance: Importance of the Loading Position

Xianqi Chen, Siping Pang, *et al.*

JUNE 23, 2023

INORGANIC CHEMISTRY

READ 

Enhancement Mechanism of Photocatalytic Hydrogen Production Activity of CeO₂/CdS by Morphology Regulation

Ziwei Liu, Haijiao Xie, *et al.*

JULY 04, 2023

ACS APPLIED ENERGY MATERIALS

READ 

Get More Suggestions >